PAPER

Neutron rate estimates in MAST based on gyro-orbit modelling of fast ions

View the article online for updates and enhancements.

Neutron rate estimates in MAST based on gyro-orbit modelling of fast ions

A. Sperduti[1] ⬤, **M. Cecconello**[1] ⬤, **S. Conroy**[1] **and A. Snicker**[2]⬤

[1] Department of Physics and Astronomy, Uppsala University, SE-751 05 Uppsala, Sweden
[2] Department of Applied Physics, Aalto University, P.O. Box 11100, 00076 AALTO, Finland

E-mail: andrea.sperduti@physics.uu.se

CrossMark

Abstract

A discrepancy between predicted and measured neutron rates on MAST using TRANSP/NUBEAM has previously been observed and a correction factor of about 0.6 was needed to match the two: this correction factor could not be accounted for by the experimental uncertainties in the plasma kinetic profiles nor in the NBI energy and power (Cecconello *et al* 2019 *Nucl. Fusion* **59** 016006). Further causes of this discrepancy are here studied by means of TRANSP/NUBEAM and ASCOT/BBNBI simulations. Different equilibria, toroidal field ripples, uncertainties on the NBI divergence value and gyro-orbit effects were studied and simulations were performed with both transport codes. It was found that the first three effects accounted for only a 5% variation in the fast ion density. On the other hand, full gyro-orbit simulations of the fast ions dynamics carried out in ASCOT/BBNBI resulted in an approximately 20% reduction of the fast ion population compared to TRANSP/NUBEAM. A detailed analysis of the fast ion distributions showed how the drop occurred regardless of the energy at pitch values $\leqslant -0.4$. The DRESS code was then used to calculate the neutron rate at the neutron camera detector's location showing that the discrepancy is considerably reduced when the full gyro-orbit fast ion distribution is used, with now the correction factor, used to match experimental and predicted neutron rates, being around 0.9.

Keywords: MAST, TRANSP/NUBEAM, ASCOT/BBNBI, fusion product deficit, fast ions

(Some figures may appear in colour only in the online journal)

1. Introduction

Obtaining an agreement on an absolute scale between measured and simulated neutron rates in present nuclear fusion devices is a challenging task both for the difficulties related to the modelling and to the diagnostic calibration. The achievement of such agreement is of crucial importance for codes and diagnostics validation in view of future burning plasma devices such as ITER and DEMO. Neutron rates are typically modelled by time-dependent codes such as TRANSP [2] coupled with the Monte Carlo fast ion module NUBEAM [3], as for example in ASDEX where agreement with measurements was obtained validating both the transport codes and the neutron diagnostic [4]. Recent detailed analyses performed on JET [5]

and on MAST [1] reported a discrepancy between the neutron emission rates predicted by TRANSP/NUBEAM and the measured ones. In particular, in MAST, a systematic discrepancy up to 40% between predicted and measured fusion products (neutrons and protons) rates (with the predicted rates much higher than the measured ones) has been observed regardless of the plasma scenarios, i.e. both in MHD quiescent and non-quiescent plasma discharges the latter being characterized by large fast ion redistribution and losses [6–8]. The interested reader can find a detailed discussion of the observed fusion products discrepancy in presence of strong MHD activity in section 4.2 of [1]. The key observation is, however, that this discrepancy is observed in absence of any MHD activity (i.e. in the so-called quiescent scenario). Plausible causes for this discrepancy were sought in the uncertainties in the plasma parameters in input to TRANSP/NUBEAM and in the

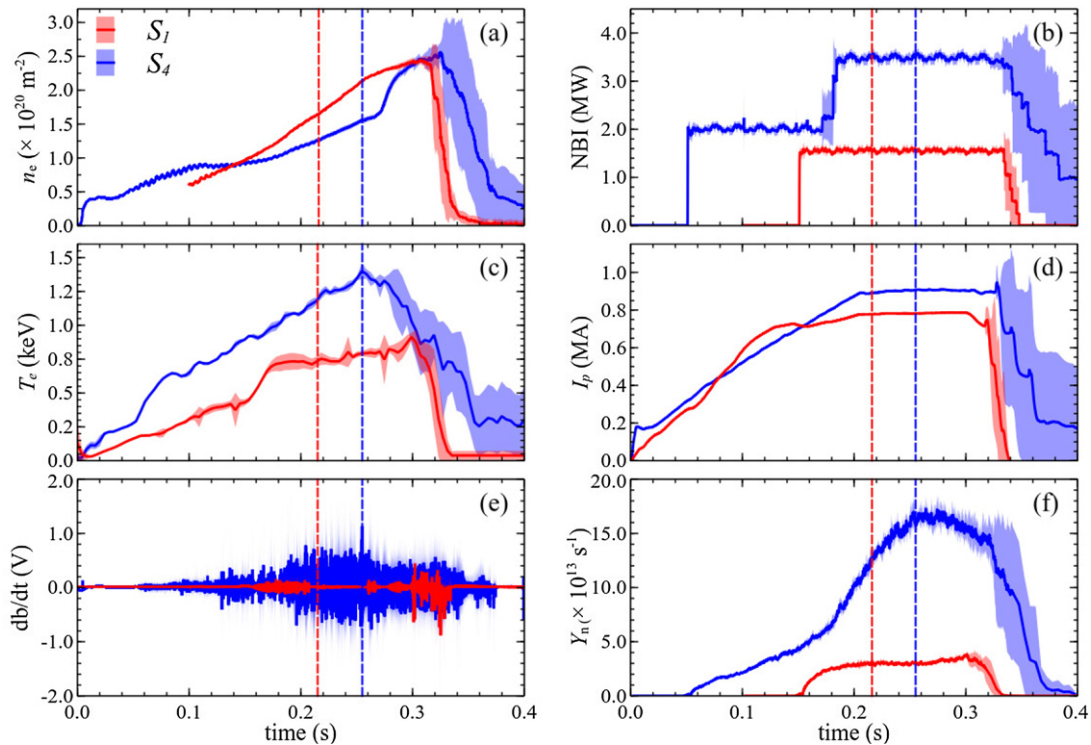* Author to whom any correspondence should be addressed.

Figure 1. Time traces for the mean values of the pulses in scenario S_1 (solid red) and S_4 (solid blue) for the line integrated electron density (*a*), the NBI heating power (*b*), the electron core temperature T_e (*c*), the plasma current I_p (*d*), the Mirnov pick-up coil signal (*e*) and the measured neutron rate by the FC (*f*). The shaded regions represent the standard deviation σ on the mean values, while the dashed lines indicate the time at which the plasma kinetic profiles were selected, $t = 0.216$ s and $t = 0.253$ s for S_1 (red) and S_4 (blue), respectively.

Table 1. Maximum percentage variation for the plasma parameters for repeated discharges calculated as $100 \times (\sigma_x/x)$, where x indicates the plasma parameter. The Mirnov signals have greater fluctuations than the other parameters due to the difficulties in reproducing the same MHD events.

Scenario	Δn_e (%)	ΔP_{NBI} (%)	ΔT_e (%)	ΔI_p (%)	$\Delta (db/dt)$ (%)	ΔY_n (%)
S_1	1.66	3.83	4.83	0.18	56.89	9.65
S_4	2.45	3.15	4.23	0.67	28.51	4.87

injected neutral beam power and found to be responsible for a variation of the neutron rate of only $\simeq 15\%$, clearly insufficient to account for the 40% discrepancy [9]. A further possible cause of the discrepancy, which was identified but not addressed in the aforementioned work, is the guiding center (GC) approximation used by NUBEAM for the calculation of the fast ion distribution. Indeed, recent works suggested that a gyro-orbit (GO) code has to be used in order to properly model the neutron emission on MAST [10, 11]. Similarly, GO codes such as ASCOT [12], LOCUST [13], OFMC [14] and SPIRAL [15] have been successfully exploited for plasma modelling on conventional and spherical tokamaks.

In this work, the results presented in [1] are reviewed taking advantage of the accelerated simulation of charged particle orbits in toroidal devices (ASCOT) GO following code in the modelling of the fast ions dynamics. ASCOT is a Monte Carlo code capable of solving the kinetic equation for fast ions, impurity species and charged fusion products both in GC motion and in full GO [12]. The GC solver is based on a fourth-order Cash–Karp Runge–Kutta integration method with fifth-order error checking while the GO integration is performed with a modified one-step leap frog scheme which conserves kinetic energy to numerical precision. ASCOT includes a beamlet-based neutral beam ionization model (BBNBI) which takes into account the geometry of the injectors and it is capable of following the injected neutrals until ionized, providing a set of markers (particles) which are then passed to ASCOT for the slowing down calculations [16]. In this study, ASCOT was used to model the fast ion distribution in MHD quiescent and non-quiescent scenarios using both GC and GO approaches. In addition, the effects on the simulated fast ion density due to toroidal field (TF) ripples, different equilibria and possible uncertainties in the neutral beam injectors (NBIs) divergence value are also here included and discussed. In particular, the effects on the fast ions due to the presence of TF ripples and to the variation in the magnetic equilibrium were tested by means of ASCOT, while the study on the NBI divergence variation was performed with TRANSP/NUBEAM.

Finally, in order to calculate the neutron rate, the simulated fast ion distributions were passed to the directional relativistic spectrum simulator (DRESS) code [17] thus allowing the comparison with experimental measurements.

This paper is organized in the following way. The reference plasma scenarios of MAST which have been studied here are presented in section 2. Section 3 describes how the TRANSP and ASCOT simulations of the fast ion distribution function for the two selected discharges were performed and the results obtained are discussed in terms of fast ion distribution densities. The comparison between the measured and the predicted neutron emissivity profiles are presented in section 4. Finally, the results are discussed and the conclusions presented in section 5.

2. Experimental setup and reference plasma scenarios

MAST [18] is a medium-sized spherical tokamak with a major radius of 0.85 m (aspect ratio $\simeq 1.3$) capable of sustaining a plasma current up to 1 MA and a plasma density of 10^{20} m^{-3} with an ion temperature up to 2 keV. The low toroidal B field ($\simeq 0.4$–0.6 T) is produced by means of 12 TF coils. Nuclear fusion reactions and current drive in MAST are sustained thanks to two tangential NBIs capable of injecting a total of 3.5 MW of neutral D with a full energy of 75 keV and an averaged initial pitch of $\lambda \approx -0.7$. Due to the low plasma temperature, the neutron emission on MAST is strongly dependent on the reaction rate between the plasma bulk deuterium and the injected fast ions, often referred to as beam-target neutrons, accounting for 90% of the total neutron emission. The remaining fraction is composed by beam–beam ($\simeq 9\%$) and thermal–thermal (less than 1%) reactions. On MAST, in order to measure spatial and time-resolved emission and energy distribution of the neutrons, and provide at the same time information about the fast ions, a fission chamber (FC) [19] and a neutron camera (NC) [20] are used. Due to uncertainties in the FC calibration, as discussed in [1], here only the experimental data from the NC are used for the benchmarking of the simulated neutron rates by DRESS. In previous studies, although a good agreement in the shape of the neutron emission profile between the measured counts and the predicted ones was found, a scaling factor $k \simeq 0.6$ was needed in order to match their absolute magnitude [9]. In order to understand the possible causes of this discrepancy, a systematic study was carried out leading to the conclusion that uncertainties in the plasma profiles in input to TRANSP/NUBEAM cannot explain this discrepancy [1]. This discrepancy was further confirmed by an independent diagnostic, the charge fusion product detector array [21] whose agreement with predicted TRANSP/NUBEAM count rates also required a similar scaling factor [1].

The analysis of the full set of scenarios selected to study the neutron deficit on MAST in [1] has not been thoroughly reproduced here, instead, two of the studied scenarios covering the two extremes of a wide range of plasma parameters have been selected. The first scenario, indicated as S_1 (including pulse numbers 29 904–29 906, 29 908–29 910) is MHD

Table 2. Maximum absolute percentage variation for the plasma kinetic profiles in the selected time windows t_{S_1} and t_{S_4} during the calculated slowing down times $t_{\tau_{S_1}}$ and $t_{\tau_{S_4}}$.

Scenario	Δn_e (%)	Δn_i (%)	ΔT_e (%)	ΔT_i (%)	$\Delta \omega$ (%)
S_1	10.3	11.3	4.8	14.8	20.2
S_4	12.8	13.5	10.1	11.4	5.3

quiescent with a 0.8 MA plasma current, a single NBI of 1.6 MW total injected power and a maximum neutron rate of $Y_n \simeq 3 \times 10^{13}$ s^{-1}. The second scenario, indicated as S_4 (pulse numbers 29 207–29 210), is characterized by a 1 MA plasma current with a total injected power of 3.3 MW, a maximum neutron rate of $Y_n \simeq 1.6 \times 10^{14}$ s^{-1} and by fishbones persisting throughout most of the discharge flat-top (figure 1(*e*)). Thanks to MAST high reproducibility, the discharges for the considered scenarios are almost identical as shown in figure 1, where the mean values of the plasma parameters are represented together with their variations in the different pulses (shaded regions). This has allowed the measurement of the neutron emissivity profile using the limited number of channels of the neutron camera. For the considered time windows in scenario S_1 and S_4, $0.215\,\mathrm{s} \leqslant t_{S_1} \leqslant 0.216\,\mathrm{s}$ and $0.252\,\mathrm{s} \leqslant t_{S_4} \leqslant 0.255\,\mathrm{s}$, respectively, the maximum absolute percentage variations in key plasma parameters are reported in table 1. Time windows around t_{S_1} and t_{S_4} have been chosen in such a way to have in that time regions stationary neutron rates as shown in panel (*f*) of figure 1.

3. Fast ion modelling

Two specific pulses, 29 909 and 29 210 belonging to scenarios S_1 and S_4, were selected to perform systematic simulation studies of the possible causes of the neutron deficit on MAST. The kinetic profiles (plasma temperature, density and rotation) used as input in both codes are obtained from the experimental data. While TRANSP/NUBEAM evolves the kinetic profiles in time, ASCOT assumes a stationary condition where the given input profiles are 'frozen' through the whole slowing down calculation. In the core plasma region of MAST, the typical slowing down time for a fast ion with an energy of 60 keV is $\tau \propto T_e^{3/2} n_e^{-1} \simeq 27$ ms [22]. For the two selected scenarios mean values of $\tau_{S_1} \simeq 21$ ms and $\tau_{S_4} \simeq 29$ ms were estimated by TRANSP/NUBEAM. This means that in order for the TRANSP-ASCOT comparison to be meaningful, the profiles used as input in TRANSP should not vary considerably in these time windows. In table 2 the maximum percentage variation of the kinetic profiles n_e, n_i, T_e, T_i, and plasma rotation ω on the magnetic axis, in $0.195 \lesssim t_{\tau_{S_1}} \lesssim 0.216$ s and $0.224 \lesssim t_{\tau_{S_4}} \lesssim 0.253$ s are reported. The percentage variation is below 15% for all the kinetic profiles, with the exception of the plasma rotation where a 20% variation is reported, resulting in an acceptable variation in the considered time windows. As regards to the magnetic equilibrium, in TRANSP this can be externally imposed or calculated using its internal free boundary equilibrium solver TEQ [23]. In ASCOT, instead, the initial equilibrium has to be provided in
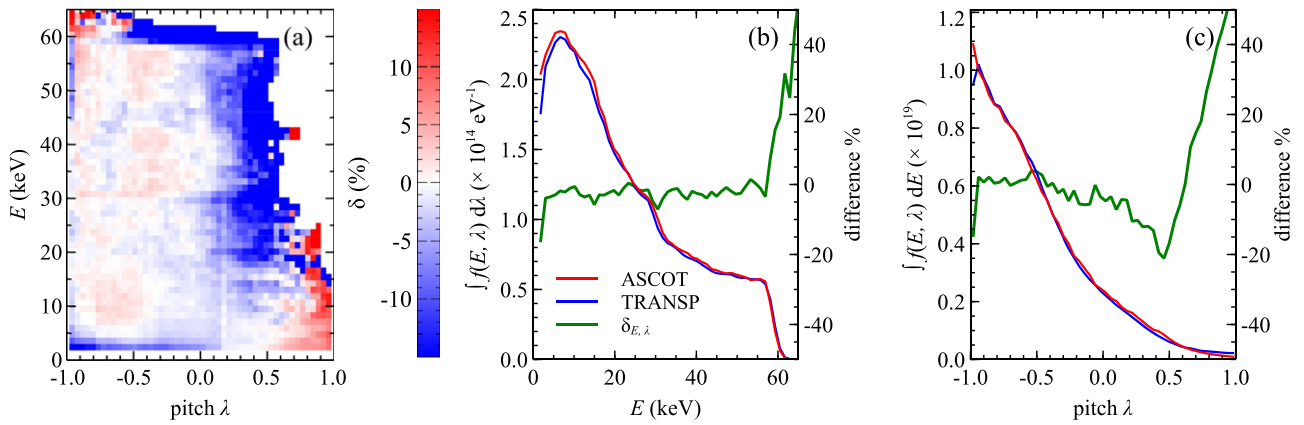
Figure 2. Panel (*a*): percentage difference between ASCOT and TRANSP fast ion distributions in energy and pitch integrated over R, Z and calculated in GC mode for MAST pulse 29 909 at $t = 0.216$ s. A positive percentage difference (red) represents a larger amount of fast ion in the TRANSP distribution, whereas a negative one means more fast ions in the ASCOT distribution (blue). Fast ion distributions integrated in pitch and in energy are shown in panels (*b*) and (*c*) together with the percentage difference $\delta_{E,\lambda}$ (green).
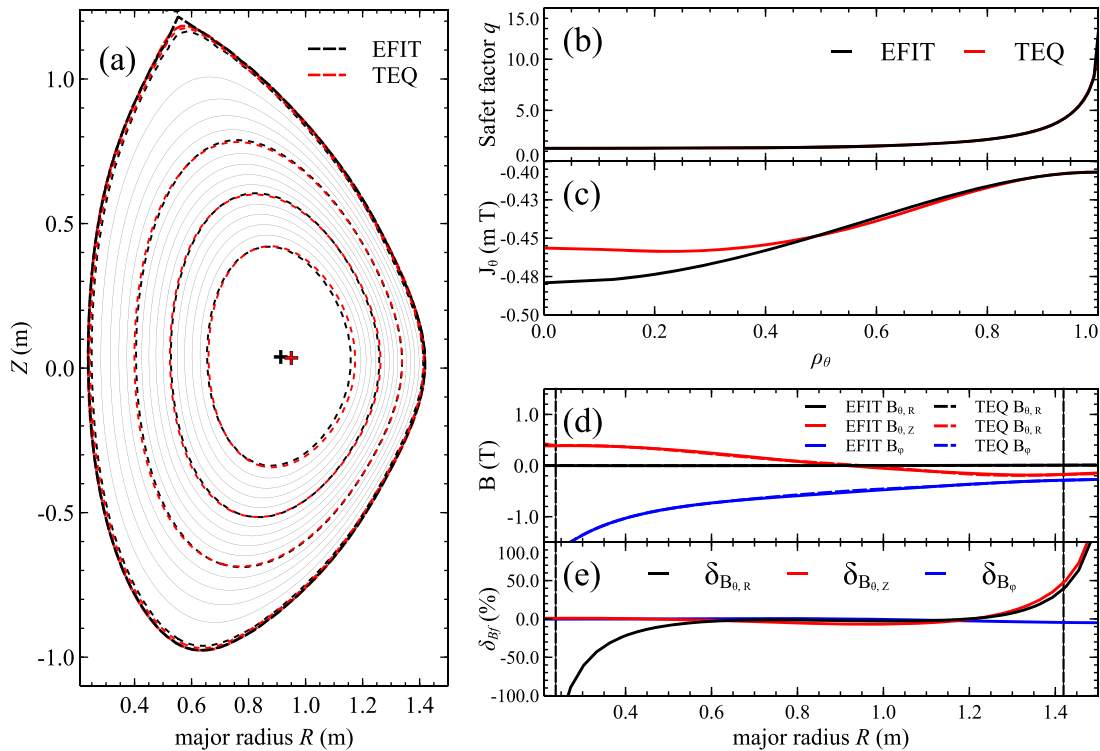

Figure 3. Magnetic fields and flux surfaces for the MAST pulse 29 909 at $t = 0.216$ s. Left panel: EFIT (dashed black) and TEQ (dashed red) contours for $\psi = (0.25, 0.5, 0.75, 1)$ (*a*). The magnetic axis are shown as well as crosses. Right panel: safety factors (*b*) and poloidal flux currents (*c*) as a function of ρ_θ for the two different equilibria. The radial profiles of the poloidal magnetic fields and the toroidal ones are shown in the bottom-right panels, where both absolute values (*d*) and percentage differences δ_{Bf} (*e*) are depicted. The dashed lines represent the positions of the inner and outer LCFS for $Z = 0$ m.

input. This is discussed more in detail in section 3.1. Since ASCOT is not able to internally evolve the magnetic equilibrium it is important for the comparison with TRANSP to ensure that, during the slowing down time, it does not change too much. From experimental measurements of the toroidal magnetic field, variations of 0.25% and 0.29% are found in the time windows $0.195 \lesssim t_{\tau_{S_1}} \lesssim 0.216$ s and $0.224 \lesssim t_{\tau_{S_4}} \lesssim 0.253$ for scenario S_1 and S_4, respectively.

Both in TRANSP and ASCOT simulations, charge exchange (CX) reactions, effective charge (Z_{eff}) and plasma rotation ω are included. TRANSP/NUBEAM simulations performed here included the finite Larmor radius (FLR) correction as well. There are mainly three major differences between the GC + FLR correction approximation in TRANSP/NUBEAM and the full GO in ASCOT: (i) in NUBEAM the point at which the physics of the slowing

down process is calculated is given by a random selection of the gyro phase angle which displaces the GC location of a Larmor radius length [3], while in the ASCOT GO simulations the gyro phase angle is randomly defined at the begin of the simulation in BBNBI and then evolved in time according to the particle GO motion, (ii) the magnetic field in TRANSP/NUBEAM is not properly modelled outside the LCFS meaning that the physical processes of the fast ions with a large Larmor radius and close to the LCFS might not be calculated properly in TRANSP/NUBEAM since the random choice of the gyro-phase angle depends on the magnetic field at the FLR location and (iii) the GC's velocity vector in TRANSP/NUBEAM is calculated assuming the conservation of the zeroth-order expression of the magnetic moment μ, that as discussed later in section 3.4, it is not conserved in MAST. The simulation terminates in both codes if any of the following conditions are met: (i) the ions slow down below $3T_i/2$, with T_i being the bulk plasma temperature and (ii) their GC or GO orbits collide with the first wall (the same 2D wall geometry was used in both codes). As regards scenario S_4, where strong MHD activity was present in the form of fishbones, an anomalous fast ion diffusion coefficient of $D_a = 2.5$ m^2 s^{-1} constant in space and velocity was included in both TRANSP and ASCOT simulations. Without such an anomalous fast ion diffusion coefficient, the scaling factor required to match measured and predicted fusion product rates in this scenario would be even smaller (approximately $k = 0.4$) compared to the quiescent plasma scenario ($k = 0.6$). An anomalous fast ion diffusion coefficient of 2.5 m^2 s^{-1} was thus introduced to account for the additional reduction in the fast ion population due to the MHD activity alone. Higher values of D_a that would reduce the discrepancy to zero ($k = 1$) are not deemed physically reasonable as discussed in [1].

TRANSP/NUBEAM computes, for a selected time slice t, the 4D fast ion velocity distribution function $f_T(R, Z, E, \lambda)$ averaged over a time interval Δt specified by the user ($\Delta t_{S_1} = 1$ ms and $\Delta t_{S_4} = 3$ ms). For the same time slice the fast ion distribution calculated by ASCOT/BBNBI is indicated as $f_A(R, Z, E, \lambda)$. The two distributions f_T and f_A were calculated on the same energy-pitch grid, while the spatial coordinates are different: TRANSP uses a 2D irregular Boozer grid [3] while ASCOT employs a regular rectangular grid. The percentage difference δ between ASCOT in GC and TRANSP fast ion distribution functions in energy and pitch and integrated in R and Z is shown in panel (a) of figure 2. Good agreement between the two distributions is found. The differences observed in the fast ion distributions for $\lambda \in [0, 0.6]$ and $E \in [20, 60]$ keV between TRANSP/NUBEAM and ASCOT/BBNBI in GC contribute very little to the total fast ion population as can be seen in panels (b) and (c). These differences might be possibly due to the different cross-section databases used to simulate the atomic processes in the two codes and the implementation of the NBI geometry. This good agreement between the two fast ion distributions in GC provides a solid starting point for the results presented and discussed in the next sections.
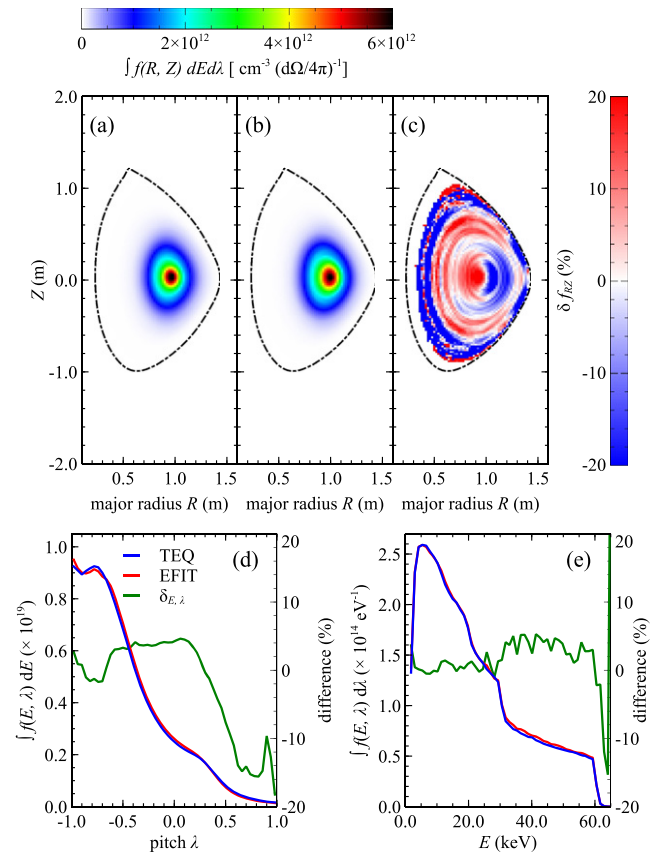

Figure 4. Fast ion distribution functions calculated by ASCOT integrated in E, λ with an EFIT equilibrium (*a*) and TEQ one (*b*). The percentage difference δf_{RZ} in shown in panel (*c*). A positive percentage difference (red) represents a larger amount of fast ion in the ASCOT distribution with the EFIT equilibrium, whereas a negative one means more fast ions in the ASCOT distribution with the TEQ equilibrium (blue). Panels (*d*) and (*e*) depict the space integrated fast ion distributions integrated in energy and in pitch, respectively. The percentage differences are shown in green.

Table 3. Summary of the simulations performed with ASCOT with the two different plasma equilibria for MAST pulse 29 909 at $t = 0.216$ s. The total number of fast ions here reported is obtained integrating the 4D fast ion distribution function $f_A(R, Z, E, \lambda)$ in all four dimensions. The percentage variation is calculated with respect to the simulation with the TEQ equilibrium.

Code	Equilibrium	Mode	n_{FI} ($\times 10^{18}$)	Variation (%)
ASCOT	TEQ	GC	3.7451	—
ASCOT	EFIT	GC	3.7945	1.32

3.1. Plasma equilibria

The effect of the magnetic equilibria calculated in two different ways for the same plasma discharge has been studied in ASCOT. For this purpose, two identical ASCOT simulations in GC have been carried out for discharge 29 909 at $t = 0.216$ s. The first one was performed using as input the magnetic equilibrium calculated by EFIT starting from pressure, current, q profile and boundary constraints [24], while the second one, was based on the TEQ magnetic equilibrium.
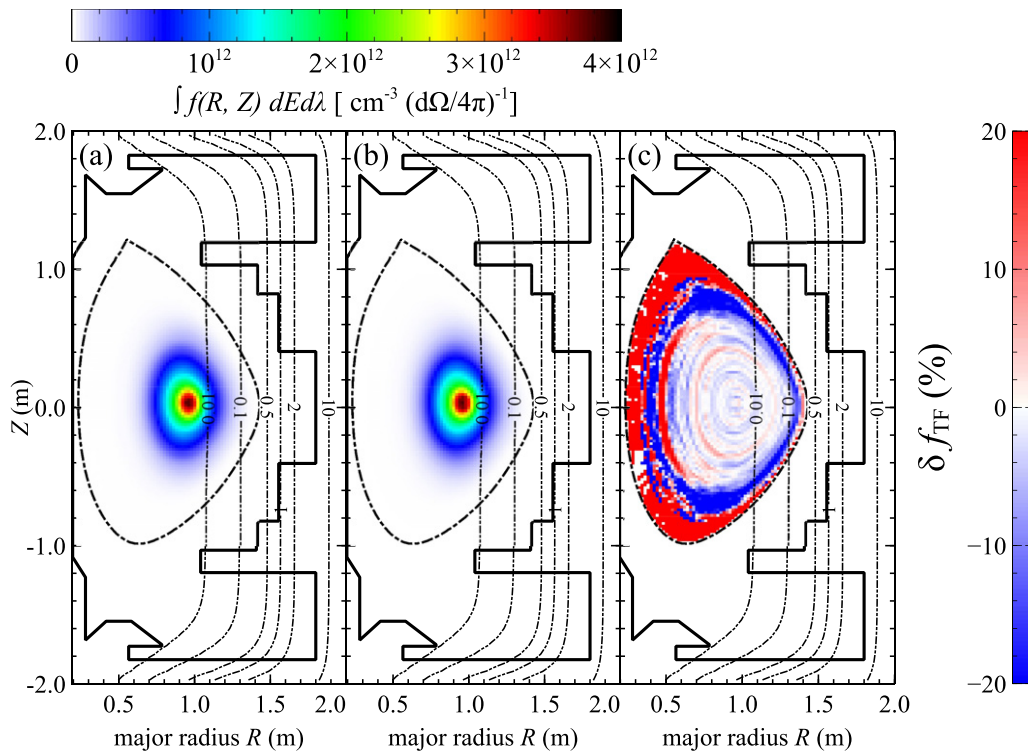
Figure 5. Fast ion distribution functions integrated in E, λ without (*a*) and with (*b*) TF ripples. The percentage difference between the two distributions is shown in panel (*c*). The magnitude of the perturbation δ_B arising from the 12 TF coils for MAST pulse 29 909 at $t = 0.216$ s are depicted as contour plots. A positive percentage difference (red) represents a larger amount of fast ion in the distribution including the TF ripples, whereas a negative one means more fast ions in the distribution without the TF ripples (blue).
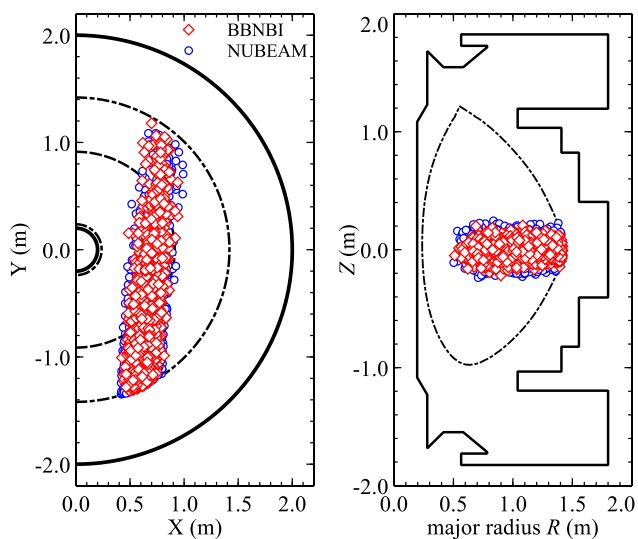

Figure 6. The D beam fast ion birth locations for the MAST pulse 29 909 at $t = 0.216$ s.

Figure 3(*a*) shows the comparison of the normalized poloidal magnetic flux of the two magnetic equilibria. Even though there are some small differences between the two equilibria (the magnetic axis and flux surfaces of the EFIT equilibrium are slightly closer to the plasma inboard side as shown in panel (*a*) of figure 3 and the poloidal flux current profile is more peaked (panel (*c*)) the magnetic field components inside the last closed flux surface (LCFS) agree quite well (panels (*d*)

and (*e*)). The corresponding fast ion distributions are shown in figure 4. Even though almost no difference is found between the fast ion distributions integrated in R, Z, where the percentage differences shown in green are well below 10% for the E, λ regions containing the largest amount of fast ions, the spatial distributions of the fast ions are quite different due to the shifting of the position of the magnetic axis. Panel (*c*) of figure 4, shows the percentage difference δf_{RZ}, where a positive percentage difference represents a larger amount of fast ion in the ASCOT distribution with the EFIT equilibrium (blue), whereas a negative one means more fast ions in the ASCOT distribution with the TEQ equilibrium (red). The fast ion distributions obtained by the two simulations were integrated over the phase-space velocity coordinates and the total number of fast ions are reported in table 3 showing very little difference and indicating that the impact of the different magnetic equilibria on the fast ion density is quite small ($\simeq 1\%$), with the ASCOT simulation performed with the EFIT equilibrium predicting a slightly greater value of fast ions. Although the fast ion density is unaffected by the different equilibria, its spatial distribution is clearly not. The effect of such a change on the spatial distribution of the fast ion population and, consequently, on the neutron emissivity will be addressed in a future work where a comparison with FIDA and NC profile measurements will be carried out. It is worth mentioning however that since most of the neutron emissivity comes from a region with $\rho_\phi \leqslant 0.6$, the net change in the fast ion spatial
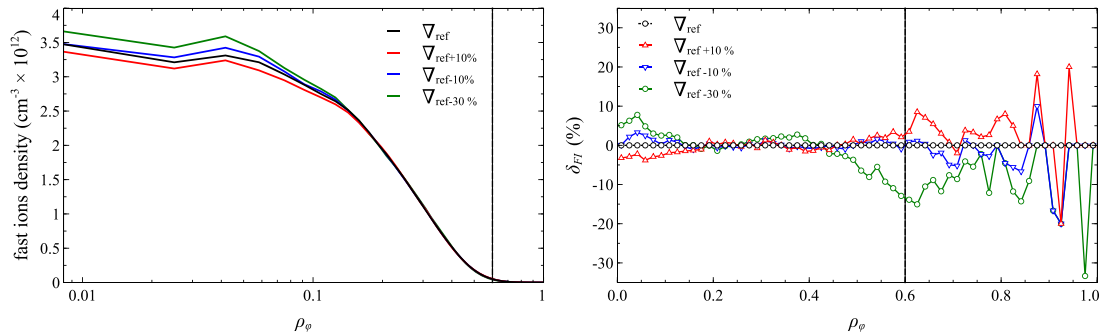
Figure 7. Left panel: semi-log plot of the fast ion density profile as a function of ρ_ϕ for the three studied case. Right panel: percentage variation of the fast ion density for the three different cases as a function of ρ_ϕ for MAST pulse 29 909 at $t = 0.216$ s. The vertical dashed line indicates the flux surface $\rho_\phi = 0.6$ inside where $\simeq 99\%$ of the fast ions are confined.

distribution is approximately zero and therefore no significant changes in the neutron rate are expected as discussed in section 4.

3.2. Toroidal field ripples

A systematic study of the effect of TF ripples on the fast ion confinement in MAST has been already performed showing that TF ripples do not contribute significantly to the fast ion losses despite the large Larmor radii of beam ions [25]. The ripple perturbation was modelled in that study as a single toroidal harmonic taking into account the magnetic field at the plasma magnetic axis, the radius of the outer vertical legs of the toroidal field coils and their number. In this study, instead, a full 3D model of the perturbation is implemented in ASCOT where the Biot–Savart law integrator [26] was used to calculate the perturbed EFIT equilibrium. The magnitude of the perturbation δ_B is calculated as

$$\delta_B(R, Z) = 100 \times |\,(B_{\max}(R, Z)$$
$$- B_{\min}(R, Z))\,/(B_{\max}(R, Z) + B_{\min}(R, Z))|, \quad (1)$$

where $B_{\max}(R, Z)$ and $B_{\min}(R, Z)$ are the maximum and minimum values of the perturbed toroidal magnetic field at (R, Z). In figure 5(c), $\delta_B(R, Z)$ is shown as a contour plot together with the percentage difference between the fast ion distributions with and without the TF ripples. The effect of the TF ripples perturbation on the initial equilibrium is found to be around $0.002\% \lesssim \delta_B \lesssim 0.3\%$ for R in the range (R_0, R_{LCFS}), the latter being the radial positions of the LCFS at $Z = 0$ m at the outer midplane. The GC simulation including the TF ripples did not show any significant difference with respect to the simulation without the perturbation in the local spatial distribution and in the total number of fast ions, while in the GO a reduction of the fast ion density of about 1% was observed compared to the simulation without TF ripples. This is due to the fact that large Larmor radii allow to experience regions of the plasma where the TF ripples perturbation has a significant effect on the fast ion orbits ($\delta_B \geqslant 0.2\%$). The fast ion distributions for the GO simulations with and without TF ripples and their percentage difference δf_{TF} are shown in figure 5. Due to the TF ripples more fast ions diffuse from the most internal regions towards the LCFS (panel (c)) than in the case without TF ripples. These

Table 4. Summary of the simulations performed with TRANSP/NUBEAM with the four different NBI divergence values for MAST pulse 29 909 at $t = 0.216$ s. The total number of fast ions here reported is obtained integrating the 4D fast ion distribution function $f_T(R, Z, E, \lambda)$ in all four dimensions. The percentage variation is calculated with respect to the reference case.

Case	Divergence	n_{FI} ($\times 10^{18}$)	Variation (%)
(i)	∇_{ref}	3.5189	—
(ii)	$\nabla_{\text{ref}+10\%}$	3.4994	−0.55
(iii)	$\nabla_{\text{ref}-10\%}$	3.5232	0.12
(iv)	$\nabla_{\text{ref}-30\%}$	3.5468	0.79

results are in agreement with those reported in [25] where for a typical MAST plasma the anomalous diffusivity due to the TF ripples was estimated to be $D_a = 0.1$ m^2 s^{-1} resulting in a $\simeq 1\%$ reduction of the fast ion density. Implementation of 3D TF ripples confirms previous results that TF ripples do not modify significantly the fast ion distribution since the fast ions are mainly confined in the plasma core where the perturbation is negligible ($\delta_B \simeq 0.002\%$).

3.3. NBI divergence

A possible source of discrepancy between NUBEAM and BBNBI is related to the way in which the NBI divergence is implemented in the two codes. The beam divergence is defined as a probability distribution function for the deflection angles α from the beamlet direction [16]. NUBEAM and BBNBI, however, use two different definitions for the Gaussian divergence. In BBNBI, α depends on the $1/e$ width of the Gaussian distribution around the beamlet axis, while in NUBEAM it depends on $1/\sqrt{e}$. This results in a $\simeq 30\%$ difference between the two divergences, but nonetheless the fast ion birth locations calculated by NUBEAM and BBNBI for MAST pulse 29 909 at $t = 0.216$ s both in equatorial and poloidal cross-sections shown in figure 6 are in good agreement, suggesting that a 30% difference in the deposition profile for MAST case does not lead to significant differences in terms of fast ion deposition profiles. However, on MAST even a small variation in the neutral beam deposition power and profile might lead to a large variation of the fast ion density and subsequently change the neutron emission. Since no uncertainty

Table 5. Estimation of the total number of fast ions contained in the fast ion distribution for each simulation performed and their percentage variation respect to the TRANSP/NUBEAM run in GC without the FLR correction, and the calculated slowing down time. The percentage variation is calculated with respect to the TRANSP/NUBEAM simulations in GC without FLR correction.

Scenario	Code	Mode	Equilibrium	n_{FI} ($\times 10^{18}$)	δn_{FI} (%)	τ (ms)
S_1	TRANSP	GC	TEQ	3.633	—	22
S_1	TRANSP	GC + FLR	TEQ	3.519	−3.13	21
S_1	ASCOT	GC	EFIT	3.706	2.01	21
S_1	ASCOT	GO	EFIT	2.960	−18.52	17
S_1	ASCOT	GO	EFIT + TF ripples	2.941	−19.04	17
S_4	TRANSP	GC + D_a	TEQ	7.682	—	30
S_4	TRANSP	GC + FLR + D_a	TEQ	7.452	−2.99	29
S_4	ASCOT	GC + D_a	EFIT + TF ripples	7.079	−7.85	28
S_4	ASCOT	GO + D_a	EFIT + TF ripples	6.193	−19.38	24

is provided for the NBI divergence on MAST, four different TRANSP/NUBEAM runs were carried out changing the beam divergence in order to estimate the sensitivity of the fast ion density on the NBI divergence. The following cases have been studied: (i) reference NUBEAM MAST's NBI divergence ∇_{ref}, (ii, iii) $\pm 10\%$ variation ($\nabla_{ref+10\%}$ and $\nabla_{ref-10\%}$) and (iv) with a BBNBI-like divergence ($\nabla_{ref-30\%}$). In figure 7 the fast ion density profiles for the four different cases are shown together with the percentage difference δ_{FI} with respect to the reference. The reason why the cases (ii) and (iii, iv) result in slightly smaller and larger fast ion density profiles compared to the reference one is due to the fact that the fast ions were mainly deposited in a plasma region with lower (ii) and higher (iii, iv) density and temperature. The fast ion distributions obtained by the four simulations were integrated over the phase-space velocity coordinates and the total number of fast ions are reported in table 4 showing very little difference and indicating that even a 30% uncertainty in the beam divergence value does not lead to a large variation of the fast ion density. The effect on the neutron emission is discussed in detail in section 4.

3.4. Guiding center vs gyro-orbit

The magnetic moment μ is one of the adiabatic invariants describing the motion of charged particles in magnetic fields. In spherical tokamaks it is well known that its zeroth-order expression μ_0 is not conserved. Large variations (up to 40%) of μ_0 are observed on MAST [27] and more in general in spherical tokamaks [28] and can be attributed to the breakdown of the condition $\frac{\nabla \mathbf{B}}{\mathbf{B}} \ll 1$. The necessity to model fast ion orbits in MAST (or in other spherical tokamaks with similar characteristics) with GO codes stems from the breakdown of this condition. In this work, to assess the impact of GC on the fast ion distribution, the two selected scenarios have been modelled with ASCOT both in GC and GO and the results compared with TRANSP/NUBEAM simulation in GC with FLR correction included. The total number of fast ions n_{FI} for all simulations are reported in table 5 together with the percentage variation

δn_{FI} calculated with respect to TRANSP/NUBEAM simulation without FLR correction (reference scenario). In scenario S_1, a small discrepancy $\delta n_{FI} \simeq -3\%$ between TRANSP with and without FLR correction is observed. In the ASCOT run in GC due to the different magnetic equilibrium and the BBNBI module (which has a slightly narrower deposition profile), an increase of the fast ion density $\delta n_{FI} \simeq 2\%$ is obtained. A much larger variation in the fast ion population ($\delta n_{FI} \simeq -20\%$) is observed with respect to the reference case when the fast ion distribution is calculated in ASCOT GO. Similar results are observed for scenario S_4, where slightly larger variations are observed between TRANSP/NUBEAM and ASCOT/BBNBI simulations in GC, mainly due to the differences in the implementation of the anomalous fast ion diffusion coefficient in the two codes, while ASCOT GO simulation predicts again a reduction of fast ions population of around $\delta n_{FI} \simeq -20\%$. This reduction in the fast ion population has been further investigated in terms of its distribution in energy, pitch and R, Z coordinates. The fast ion distributions calculated by ASCOT in GC and GO for scenario S_1 and integrated in space and velocity coordinates are shown in figures 8 and 9, respectively. The difference between the two fast ion distributions is noticeable. Most of the fast ion reduction in the GO case comes from passing particles with $\lambda \lesssim -0.4$ (panel (c) of figure 8), a pitch close to the passing-trapped boundary on MAST [27, 29]. Two energy regions in the fast ion distribution limited by $-1 \lesssim \lambda \lesssim -0.4$ are considered. In the low energy region $E \lesssim 30$ keV the reduction of the fast ion density compared to the GC is mainly due to the increase of first wall collisions, CX reactions and recombination losses particularly outside the LCFS. The presence of the Larmor radius in the GO simulations causes the fast ions to experience wider orbits which can then interact with neutrals outside the LCFS. Instead, in the high energy region $E > 30$ keV, the fast ions in the GO simulations are lost due to wall collisions. Similar simulations of the beam loss fraction in NSTX predicted around 20% fast ion losses at full-energy [30]. The increase of physical reactions in the GO simulations has as main consequences the reduction of the fast ion populations and a shorter slowing down time of the
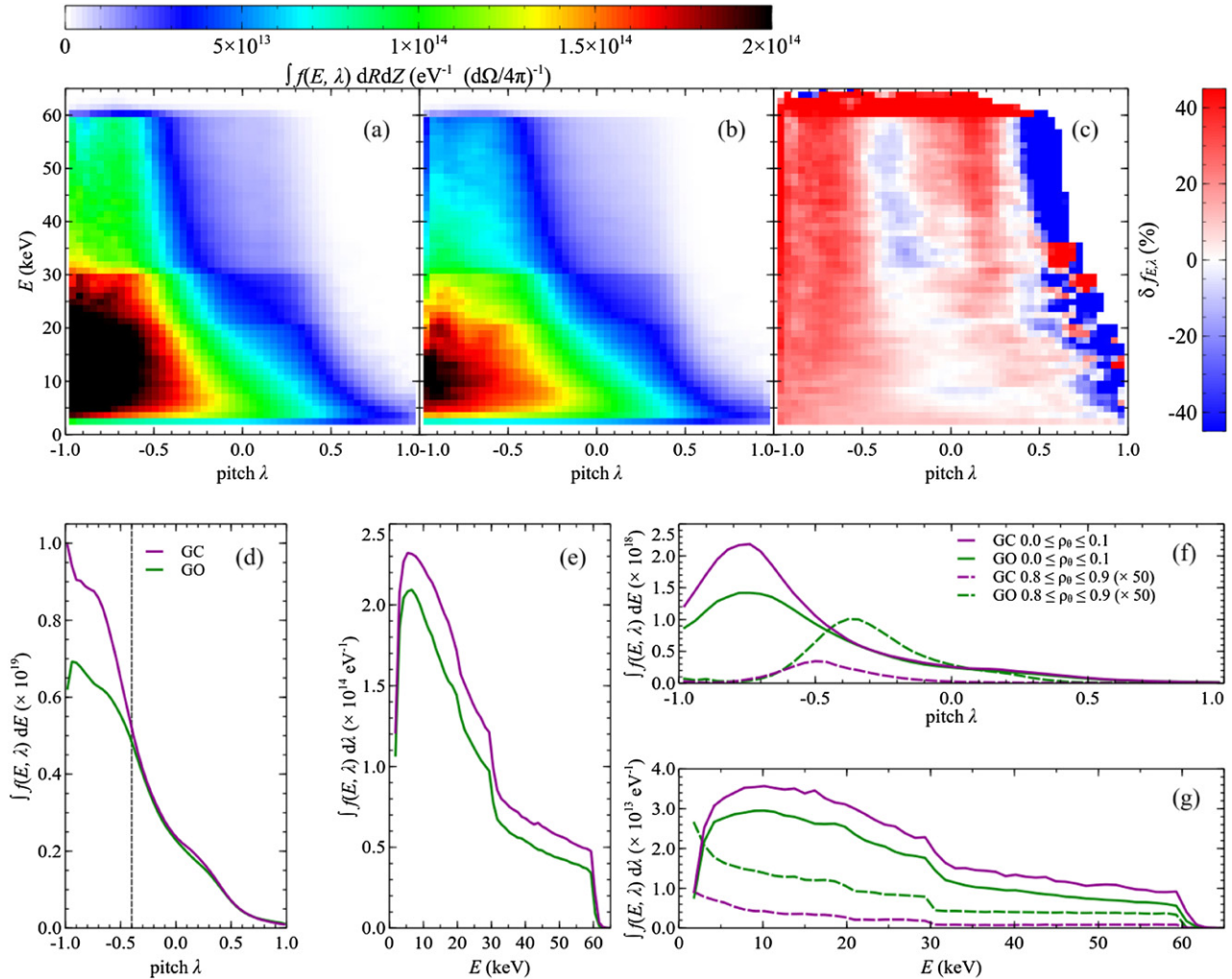
Figure 8. MAST pulse 29 909 at $t = 0.216$ s fast ion distributions in (E, λ) obtained with ASCOT-GC (*a*) and ASCOT-GO (*b*). The percentage difference between the two distributions is shown in panel (*c*). A positive percentage difference (red) represents a larger amount of fast ion in the GC distribution, whereas a negative one means more fast ions in the GO distribution (blue). The integrated distributions in energy and in pitch are shown in panel (*d*) and (*e*), respectively. The dashed line indicates $\lambda = -0.4$. In panel (*f*) and (*g*) are depicted the fast ion distributions integrated between $0.0 \leqslant \rho_\theta \leqslant 0.1$ (solid) and $0.8 \leqslant \rho_\theta \leqslant 0.9$ (dashed) and in energy, panel (*f*) and in pitch, panel (*g*).

fast ions (τ_{GO}) compared with that calculated in GC simulations (τ_{GC}). Values of τ_{GO} shorter than τ_{GC} reported in table 5 are comparable with results observed in previous works [10].

Albeit the fast ion density reduction in the GO calculations is the predominant effect, a different spatial distribution is also present as shown in figure 9. In particular, close to the inner and outer LCFS an increment of the total number of fast ions is observed, suggesting that in GO mode the fast ions due to the large Larmor radius are able to experience very different values of the magnetic field due to the large gradient compared to the fast ions in the GC mode. This is shown in figures 8(*f*) and (*g*), where the fast ion distributions are integrated in two different spatial regions: (i) $0.0 \leqslant \rho_\theta \leqslant 0.1$ and $0.8 \leqslant \rho_\theta \leqslant 0.9$. Clearly, a large fraction of the fast ion losses shown in figures 8(*d*) and (*e*) come from the plasma core where a strong reduction is observed for $-1 \leqslant \lambda \leqslant -0.5$. In the second region, an increment of fast ions in GO orbit is observed, where due to the large Larmor radii the fast ions are diffused towards the LCFS.

4. Neutron rate calculations with DRESS

The computed fast ion distributions are passed to the DRESS code [17] together with the information regarding the reactants (temperature, density, rotation velocity) and the equilibrium magnetic field to calculate the global and local neutron emission for comparison with experimental measurements. First, the effects of different plasma equilibria, TF ripples and uncertainty on the NBI divergence on MAST neutron emission were studied. DRESS calculated the neutron emissivity using the fast ion distributions discussed in sections 3.1 (EFIT and TEQ equilibria) and 3.2 (with and without TF ripples). For the different magnetic equilibria, an increase of $\simeq 2\%$ in the neutron emission was observed for the case with the EFIT equilibrium with respect to the TEQ one, while for the case including the TF ripples a reduction of $\simeq 1\%$ in the neutron emission compared to the case without TF ripples was observed.

The uncertainty on the NBI divergence was studied in terms of neutron emission components as shown in panels (*a*) and (*b*)
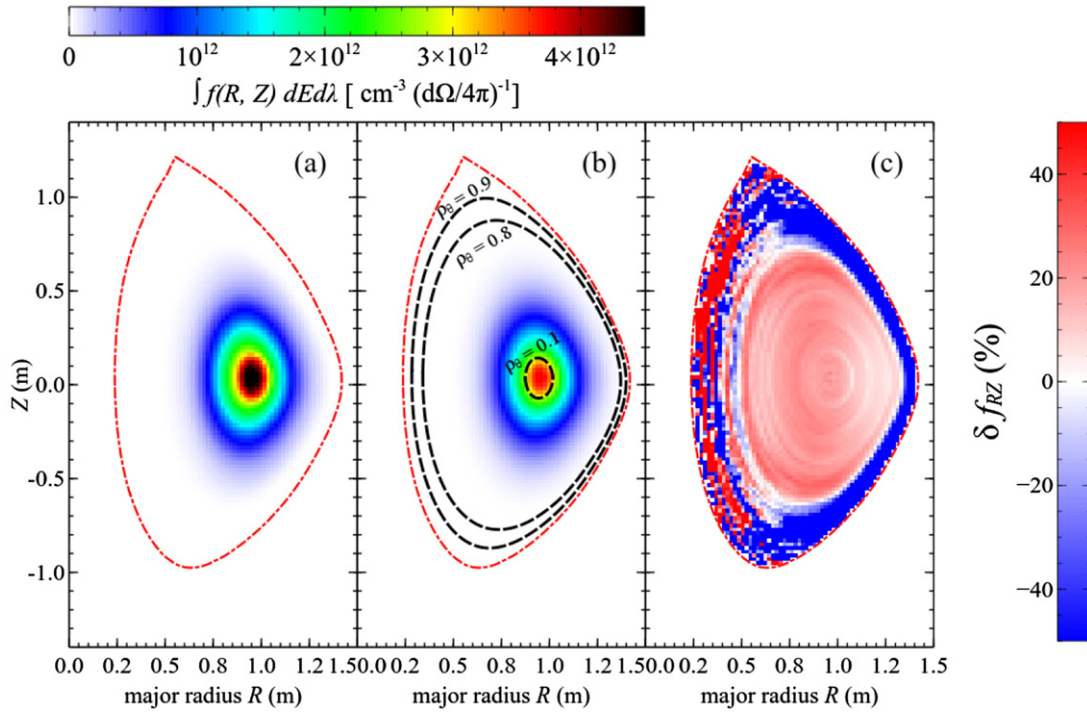
Figure 9. MAST pulse 29 909 at $t = 0.216$ s fast ion distributions in (R, Z) obtained with ASCOT-GC (*a*) and ASCOT-GO (*b*). The percentage difference is shown in the panel (*c*), where a positive percentage difference (red) represents a larger amount of fast ion in the GC distribution, whereas a negative one means more fast ions in the GO distribution (blue). The flux surfaces with $\rho_\theta = 0.1$, 0.8 and 0.9 are shown in dashed black while the LCFS in dashed red.
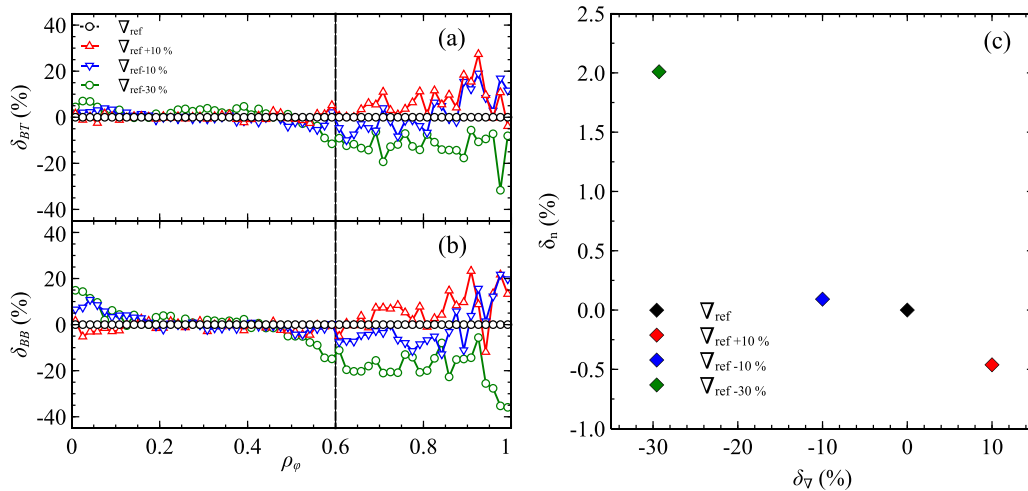

Figure 10. MAST pulse 29 909 at $t = 0.216$ s: the percentage variation of the beam–thermal (*a*) and beam–beam (*b*) components computed by NUBEAM for the five different cases as a function of ρ_ϕ. The beam–beam component is more affected by the variation in the beamlet divergence. The dashed lines indicate the limit of the plasma region enclosed by the flux surface $\rho_\phi = 0.6$ from where all beam–thermal and beam–beam neutrons ($\simeq 99\%$) are emitted. Right panel (*c*) shows the neutron rate variation due to the change in the beamlet divergence.

of figure 10. The percentage variation of the beam–thermal δ_{BT} and beam–beam δ_{BB} components are depicted as a function of ρ_ϕ: the largest effect due to the divergence variation is observed in the beam–beam component for the case $\nabla_{\text{ref}-30\%}$ where close to the magnetic axis a more peaked neutron beam–beam emission profile is observed as a consequence of the smaller divergence implemented in BBNBI. The total neutron rates Y_n for the four different cases were normalized to the neutron rate for the reference case and the percentage difference δ_n is

shown in panel (*c*) of figure 10 as a function of the percentage difference of the beam divergence δ_∇ with respect to the reference one. As can be seen the different implementation of the NBI divergence in NUBEAM and BBNBI does not lead to a huge variation in the neutron rate ($\simeq 2\%$), suggesting that this and the aforementioned effects do not contribute significantly to the neutron discrepancy observed on MAST.

In order to calculate the neutron rate at NC's detectors location, the LINE21 code [31] was coupled to DRESS. The
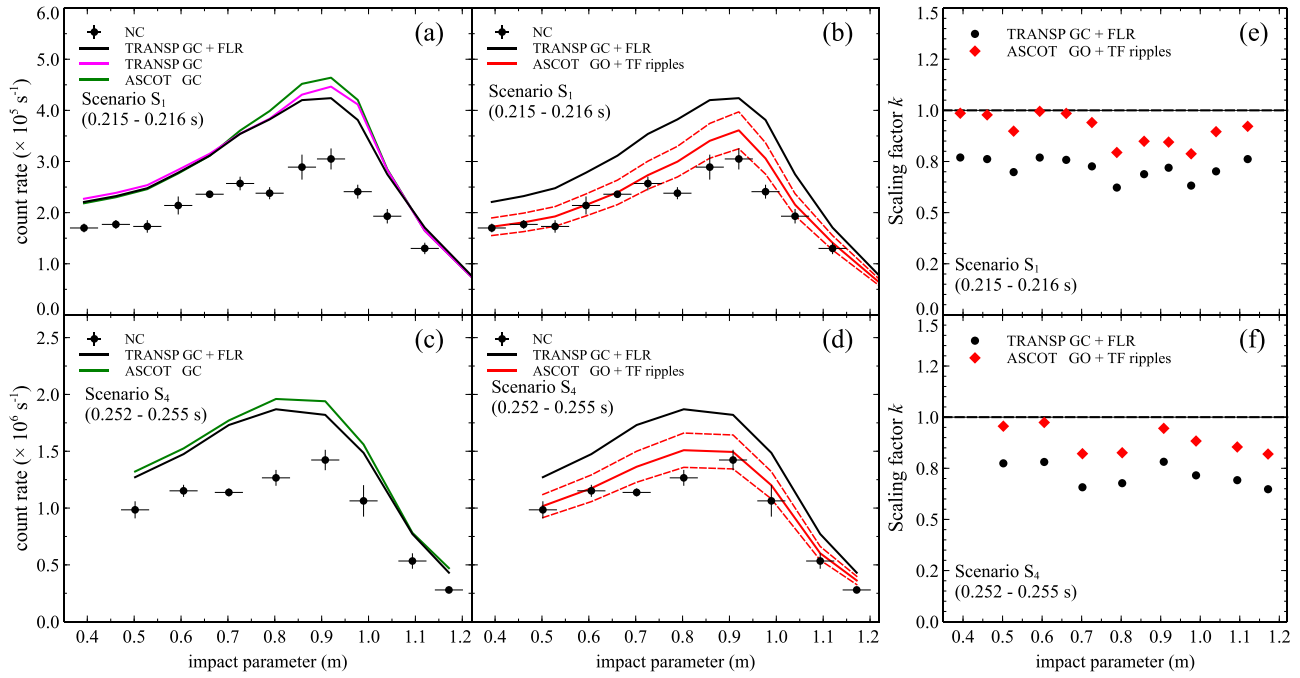
Figure 11. Comparison between the measured (solid circles) and the predicted by TRANSP GC, TRANSP GC + FLR and ASCOT GC (continuous line) neutron camera CRs for scenario S_1 (a) and S_4 (c). In (b) (S_1) and (d) (S_4) are shown the predicted CRs by ASCOT GO + TF ripples and TRANSP GC + FLR and again the measured ones. The red dashed lines are the uncertainties on the predicted CRs by ASCOT GO + TF ripples resulting from the average uncertainty in the input plasma profiles. Panels (e) and (f) show the comparisons between the scaling factor k for the TRANSP GC + FLR simulation and that one obtained using ASCOT GO + TF ripples for scenario S_1 and S_4. The black dashed line indicates $k = 1$ which would mean a perfect agreement between the predicted and the measured CRs.

Table 6. Estimation of the scaling factor for the analyzed scenarios.

Scenario	Code	Mode	Equilibrium	$k \pm \sigma_k$	$\overline{k} \pm \sigma_{\overline{k}}$	R^2
S_1	TRANSP	GC + FLR	TEQ	0.72 ± 0.01	0.744 ± 0.004	0.853
S_1	ASCOT	GO	EFIT + TF ripples	0.91 ± 0.02	0.923 ± 0.006	0.819
S_4	TRANSP	GC + D_a + FLR	TEQ	0.71 ± 0.01	0.695 ± 0.008	0.971
S_4	ASCOT	GO + D_a	EFIT + TF ripples	0.88 ± 0.02	0.875 ± 0.009	0.940

observed count rates (CRs) profiles for the NC and those predicted with DRESS using as input the fast ion distributions simulated by ASCOT and TRANSP are shown in figure 11 for both S_1 and S_4 scenarios. Panels (a) and (c) depict the neutron emissivity profiles obtained by TRANSP and ASCOT in GC, showing how the GC approximation overestimates the measured CR similarly to the results in [1]. Panels (b) and (d) show instead the predicted CRs using the fast ion distribution calculated in ASCOT GO + TF ripples together with the experimental measurements. The simulated CRs in GC with the FLR correction by TRANSP are shown again in panels (b) and (d) for visual comparison purposes. The shape of the simulated profile in panel (b) is slightly modified by the GO, especially for impact parameters between 0.8 and 1.0 m. The absolute magnitudes of the predicted profiles are in better agreement with the experimental ones, strengthening the validity of the results here reported and suggesting that GO calculations better describe the fast ion distribution dynamics in spherical tokamaks.

For each impact parameter and for both scenarios, the scaling factors k needed to match the predicted values CR_p with the measured ones CR_m (where indexes 'p' and 'm' denotes predicted and measured) are calculated as $k = \frac{CR_m}{CR_p}$ and shown in panel (e) and (f) of figure 11. These calculations are summarized in table 6 where the mean values are reported together with uncertainties for both scenarios. The scaling factor k calculated in this way is the ratio of two random variables and this ratio might not be normally distributed. Therefore, a weighted least square regression fit $CR_m = \overline{k}CR_p$ was performed. The weights in the fit are given by the experimental uncertainties in CR_m. The results are reported in table 6 together with uncertainties and correlation coefficients R^2 and shown in figure 12. The predicted CRs by ASCOT and TRANSP for scenario S_1 are in better agreement with the measured ones than those in scenario S_4. This is possibly due to the strong MHD activity present in the non-quiescent scenario. The redistribution of fast ions via the anomalous fast ion diffusion coefficient used in both TRANSP and ASCOT simulations does
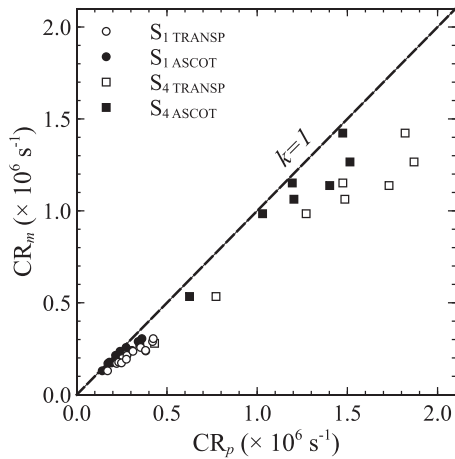
Figure 12. Comparison between the TRANSP and ASCOT predicted count rates CR$_p$ and measured CR$_m$. The dashed black line represent a perfect agreement between the predicted and the measured CRs ($k = 1$).

not contain a physical description of the interaction between MHD instabilities and fast ions and therefore it is a crude oversimplification.

5. Discussion and conclusions

A series of TRANSP/NUBEAM and ASCOT/BBNBI simulations have been performed both for an MHD quiescent and non-quiescent scenario to understand the possible causes of the neutron deficit observed on MAST which was found to be independent on the plasma scenario and of the order of 40%. In this work, it has been shown that this discrepancy can not be due to TF ripples, different plasma equilibria and NBI divergence implemented in two codes since all these effects together can account only for a $\simeq 5\%$ variation in the total neutron emission rate. To assess the impact of gyro orbits, the ASCOT code has been used since it can be run in both GC and GO for the same equilibrium and kinetic profiles. Since these are implemented in a different way compared to TRANSP, the first step has been the benchmarking of ASCOT GC with TRANSP with FLR correction resulting in a good agreement in terms of the total number of fast ions. GC and GO simulations were then performed with ASCOT/BBNBI and a difference in the fast ion density of about 20% was found for both studied scenario. A detailed analysis of how the two fast ion distributions depend on the phase space and velocity coordinates was carried out. The results here reported show how the GO dramatically changes the fast ion distribution both in energy-pitch and R, Z resulting in a reduction of the fast ions for $\lambda \leqslant -0.4$ and in the plasma core, regardless of the energy due to CX reactions and wall collisions. These results are in agreement with what has been observed in the past on MAST by means of independent GO codes [10, 11]. Finally, it is worth mentioning that the boundary used in ASCOT to represent the limiters, divertors and poloidal field coils is an approximation of the real geometry. This can be appreciated by comparing the boundary used in ASCOT and shown in figure 5 with the one shown in panel (*a*) of figure 2 of reference [1]. The continuous nature

of the closed boundary used in ASCOT, however, is not the cause of the reduction in the fast ion population. This has been verified by evaluating the fast ion density when replacing the outboard boundary with a straight vertical boundary located at $R = 2$ m: the difference in the fast ion population with respect to the original boundary was less than 1%. The impact of the fast ion populations thus calculated on the neutron count rates have been simulated by means of DRESS and compared with those measured by the neutron camera. A discrepancy between the two values is still present being now in the order of $\simeq 10\%$ for the two selected scenario rather than the 40% reported in [1]. These results suggest that the GO is more suitable for the calculation of the fast ion transport simulations in spherical tokamaks since the GC it is not able to predict correctly the losses and the distribution function due to the combination between a low **B** field and of large ∇**B** leading to the neutron deficit recently observed in [1] even with the inclusion of the FLR correction.

ORCID iDs

A. Sperduti https://orcid.org/0000-0002-9911-1549
M. Cecconello https://orcid.org/0000-0002-2571-1920
A. Snicker https://orcid.org/0000-0001-9604-9666

References

[1] Cecconello M., Boeglin W., Keeling D., Conroy S., Klimek I. and Perez R.V. 2019 *Nucl. Fusion* **59** 016006
[2] Goldston R.J. *et al* 1981 *J. Comput. Phys.* **43** 61
[3] Pankin A., McCune D., Andre R., Bateman G. and Kritz A. 2004 *Comput. Phys. Commun.* **159** 157
[4] Tardini G., Höhbauer C., Fischer R. and Neu R. ASDEX Upgrade Team 2013 *Nucl. Fusion* **53** 063027
[5] Weisen H. *et al* 2017 *Nucl. Fusion* **57** 076029
[6] Turnyanskiy M., Keeling D.L., Akers R.J., Cunningham G., Conway N.J., Meyer H., Michael C.A. and Pinches S.D. 2009 *Nucl. Fusion* **49** 065002
[7] Turnyanskiy M. *et al* 2013 *Nucl. Fusion* **53** 053016
[8] Keeling D.L. *et al* 2015 *Nucl. Fusion* **55** 013021

[9] Klimek I. *et al* 2015 *Nucl. Fusion* **55** 023003

[10] McClements K.G., Tani K., Akers R.J., Liu Y.Q., Shinohara K., Tsutsui H. and Tsuji-Iio S. 2018 *Plasma Phys. Control. Fusion* **60** 095005

[11] Tani K. *et al* 2016 *Plasma Phys. Control. Fusion* **58** 105005

[12] Hirvijoki E., Asunta O., Koskela T., Kurki-Suonio T., Miettunen J., Sipilä S., Snicker A. and Äkäslompolo S. 2014 *Comput. Phys. Commun.* **185** 1310

[13] Akers R.J., Verwichte E., Martin T.J., Pinches S.D. and Lake R. 2012 *39th EPS Conf. Plasma Physics* (Stockholm, Sweden, 2–6 July 2012) P5.088 (http://ocs.ciemat.es/epsicpp2012pap/pdf/P5.088.pdf)

[14] Tani K., Azumi M., Kishimoto H. and Tamura S. 1981 *J. Phys. Soc. Jpn.* **50** 1726

[15] Kramer G.J., Budny R.V., Bortolon A., Fredrickson E.D., Fu G.Y., Heidbrink W.W., Nazikian R., Valeo E. and Van Zeeland M.A. 2013 *Plasma Phys. Control. Fusion* **55** 025013

[16] Asunta O., Govenius J., Budny R., Gorelenkova M., Tardini G., Kurki-Suonio T., Salmi A. and Sipilä S. 2015 *Comput. Phys. Commun.* **188** 33

[17] Eriksson J., Conroy S., Andersson Sundén E. and Hellesen C. 2016 *Comput. Phys. Commun.* **199** 40

[18] Herschbach K., Maurer W. and Vetter J.E. 1995 *Fusion technology 1994 Proceedings* vol 1 (https://inis.iaea.org/search/search.aspx?orig_q=RN:27049467)

[19] Stammers K. and Loughlin M.J. 2006 *Nucl. Instrum. Methods Phys. Res.* A **562** 521

[20] Cecconello M. *et al* 2014 *Nucl. Instrum. Methods Phys. Res.* A **753** 72–83

[21] Perez R.V. *et al* 2014 *Rev. Sci. Instrum.* **85** 11D701

[22] Stix T.H. 1972 *Plasma Phys.* **14** 367

[23] Degtyarev L. and Drozdov V. 1985 *Comput. Phys. Rep.* **2** 341–87

[24] Lao L.L., Ferron J.R., Groebner R.J., Howl W., St. John H., Strait E.J. and Taylor T.S. 1990 *Nucl. Fusion* **30** 1035

[25] McClements K.G. and Hole M.J. 2012 *Phys. Plasmas* **19** 072514

[26] Äkäslompolo S. *et al* 2015 arXiv:1511.01629

[27] Cecconello M. and Sperduti A. 2018 *Plasma Phys. Control. Fusion* **60** 055008

[28] Carlsson J. 2001 *Phys. Plasmas* **8** 4725

[29] Michael C.A. *et al* 2013 *Plasma Phys. Control. Fusion* **55** 095007

[30] Egedal J., Redi M.H., Darrow D.S. and Kaye S.M. 2003 *Phys. Plasmas* **10** 2372

[31] Conroy S. 2009 private communication